Advanced Materials Interfaces

ADVANCED MATERIALS INTERFACES Open Access

www.advmatinterfaces.de

RESEARCH ARTICLE OPEN ACCESS

3D-Printed Arch-Structured Tribolayer with Conducting Polymer Coating for Enhanced Triboelectric Energy Harvesting

Mariam E. Alhosani[1,2] | Bushara Fatma[3] | Reem B. Irshaid[1,4] | Kyriaki Katsikari[4] | Maryam Aljaberi[1] | Israr Ud Din[3,5] | Seoyoung Kang[6] | Young Pyo Jeon[6] | Kamran A. Khan[2,3] | Charalampos Pitsalidis[2,4]

[1]Department of Biomedical Engineering, Khalifa University of Science and Technology, Abu Dhabi, UAE | [2]Advanced Research and Innovation Center (ARIC), Khalifa University of Science and Technology, Abu Dhabi, UAE | [3]Department of Aerospace Engineering, Khalifa University of Science and Technology, Abu Dhabi, UAE | [4]Khalifa University of Science and Technology, Abu Dhabi, UAE | [5]Brunel Composites Centre, College of Engineering, Design and Physical Sciences, Brunel University of London, Kingston Lane, Uxbridge, London, UK | [6]Research For Advanced Institute of Convergence Technology, Seoul National University, Gyeonggi-do, Republic of Korea

Correspondence: Charalampos Pitsalidis (Charalampos.pitsalidis@ku.ac.ae)

Received: 20 October 2025 | **Revised:** 13 February 2026 | **Accepted:** 17 February 2026

Keywords: 3D-printing | conducting polymer | PEDOT:PSS | TENG | triboelectric nanogenerators

ABSTRACT

Three-dimensional printed (3DP) triboelectric nanogenerators (TENGs) provide a versatile approach for complex and customizable microstructures tailored for efficient energy harvesting and sensing. Here, we demonstrate the fabrication of flexible microstructured TENGs produced via stereolithography 3D printing and subsequently coated with a conducting polymer, PEDOT:PSS (P:P). Three geometries are investigated: pillars, pyramids, and arches, with the arch configuration emerging as a new design combining enhanced mechanical adaptability and improved triboelectric performance. The arch-shaped TENGs exhibit superior flexibility, structural stability, and a high active surface area, which collectively facilitate efficient energy conversion under repetitive deformation. Furthermore, the incorporation of P:P coating substantially enhances performance, resulting in a more than twentyfold increase in voltage output compared to uncoated counterparts. Among the 3DP structures, the arch geometry consistently delivers better performance, confirming the geometry-driven performance of 3DP-TENGs. The optimized arch configuration is found to yield a peak voltage output of ~101 V, corresponding to a maximum power output of ~193.6 mW/m^2. By exploiting the spring-like behavior of the arch-shaped tribolayer, a "zero-gap" TENG architecture is presented, offering a compact and adaptable energy-harvesting platform as well as pressure-sensing capabilities. Finally, a wireless pressure-sensing platform configured as a vehicle parking counter is demonstrated, showcasing the potential of this development for integration into smart infrastructure and environmental monitoring systems.

1 | Introduction

Over the last decade, advances in materials science, nanotechnology, and device engineering have led to the development of new solutions in sustainable energy and self-powered devices [1]. The resulting developments have introduced new materials and device approaches that have enabled efficient energy harvesting from various environmental sources and biomechanical activities

Mariam E. Alhosani and Bushara Fatma contributed equally to this paper.

[2]. This progress is driving sustainable solutions for power generation and opening up applications in fields ranging from wearable electronics and biomedical devices to remote sensing and environmental monitoring. Among various energy harvesters, triboelectric nanogenerators (TENGs) undoubtedly represent one of the most promising technologies to have emerged, revolutionizing wearable [3, 4] and textile electronics [5, 6] as well as green energy applications [7–9]. TENGs can typically capture distributed and irregular low-frequency mechanical energy from surrounding sources, such as vibrations and human motion, converting it into electrical power [10–12]. While the primary operating principle of TENG is well studied and understood, the theoretical explanation is still under investigation [13, 14]. Studies have demonstrated that TENG's operation is based on contact electrification and electrostatic induction coupling [15]. The dynamic interaction between different material surfaces causes fluctuations in potential difference, which induce a flow of electrons within the external circuit as the surfaces repeatedly make and break contact. As such, alterations in the surface chemistry, charge density, roughness, and microarchitecture of the functional layers can significantly impact the device's performance [16–19]. Coupling materials with a difference in electron affinity, as well as employing micro/nanotextured surfaces, is a common strategy, as these characteristics can enhance charge generation and maximize power output. Specifically, the electron affinity difference increases the tendency for electron transfer upon contact, thereby amplifying the contact electrification effect. Meanwhile, surface texture and roughness can increase the active contact area between the two tribolayers, allowing for more points of interaction and enhancing the charge transfer capacity of the device [11, 17, 20, 21]. The multiple variables introduced with TENG technology allow for numerous material combinations, with polymers and nanomaterials being particularly promising [9].

TENGs frequently use structured surfaces, such as micropatterned electrodes, gratings, or nanostructured layers, to enhance electrification effects and charge interactions [22–24]. Nevertheless, fabricating these nano-/micropatterned domains and geometries often requires advanced manufacturing techniques, such as photolithography, which can be complex and costly. Apart from that, these techniques may compromise the scalability and deployment in large-scale manufacturing. Recently, additive manufacturing has made considerable advancements in the development of energy harvesters [25], including TENGs, driven by new manufacturing techniques, designs, and innovations in printing materials [26–30]. This has enabled the precise fabrication of patterns and micro/nanostructures with a complexity level on par with other fabrication techniques (i.e., soft lithography). To date, researchers have extensively explored a diverse range of commercial materials using fused deposition modeling (FDM) [30, 31], direct ink writing (DIW) [32–34], and resin-based printing methods, such as stereolithography (SLA) [35] and digital light processing (DLP) [26]. While FDM and DIW offer a versatile, easy-to-print, and more environmentally friendly approach, they generally lack resolution, and 3DP design precision is rather limited. On the other hand, resin-based 3D printing methods utilize photopolymer resins, offering tailorability and producing highly detailed 3D printouts. In addition, several resin formulations have been developed to date, including biocompatible, high-strength, and flexible resins, broadening the range of applications for 3DP-structures [26, 36]. Beyond the choice of resin material, 3DP architectures are frequently coated or modified with additional materials to improve their mechanical performance, stability, or specific functional response, thereby tailoring them for targeted applications, such as those of TENGs.

Building on this, a common strategy to enhance TENG performance involves the use of functional coatings to optimize charge generation, mechanical responsiveness, durability, and overall energy conversion efficiency [37–39]. Incorporating polymers or functional molecules can tune their surface charge affinity by modifying electron-donor/acceptor behavior during contact electrification. Conducting polymers, such as polypyrrole and poly(3,4-ethylenedioxythiophene):poly(styrene sulfonate) (PEDOT:PSS; P:P), have been used in TENGs [40–43], typically employed as a charge-enhancing transport layer [44, 45]. While these studies have explored the use of conducting polymers to enhance the performance of TENGs, the integration of such materials with 3DP-TENGs remains rather unexplored.

In this work, we present the development of flexible 3DP TENGs fabricated through a dual-processing approach, in which microstructured tribolayers are produced via stereolithography 3D printing using a commercial polyurethane (PU)-based resin subsequently spray-coated with a P:P film. To investigate the structure–performance relationship, three 3D microstructure geometries, such as pillars, pyramids, and arches, are designed and fabricated with distinct dimensional features and identical material compositions. Pillars known to deform primarily through axial compression and bending, resulting in rather irregular contact during stress and a limited effective contact area. Pyramids place stress at their tips, increasing local pressure but reducing contact area and increasing stiffness. In contrast, the newly introduced feature in our study, arches, is found to distribute stress over a large surface, enabling gradual contact formation, greater mechanical adaptability, improved stability, and superior durability under repeated loading. Overall, the three geometries represent fundamentally different mechanical deformation modes, allowing a rational comparison of how geometry and conductive-polymer functionalization together influence energy conversion. In all cases, the incorporation of a P:P coating is found to substantially enhance the electrical output of the TENGs, demonstrating its effectiveness as a general strategy for boosting performance in TENGs. The presented approach offers a design strategy for future geometry-driven optimization of 3DP TENGs.

2 | Results and Discussion

2.1 | 3DP Microstructured Tribolayers

SLA types of 3D printing enable the fabrication of accurate and precise structures at the micron scale. With a resolution of a few tens of μm, it enables the formation of multiplanar features essential for applications requiring smooth surface patterns with variable aspect ratios. Exploiting this capability, a stepwise approach is employed to fabricate microstructured 3DP tribolayers, as shown in Figure 1a. After designing the desired

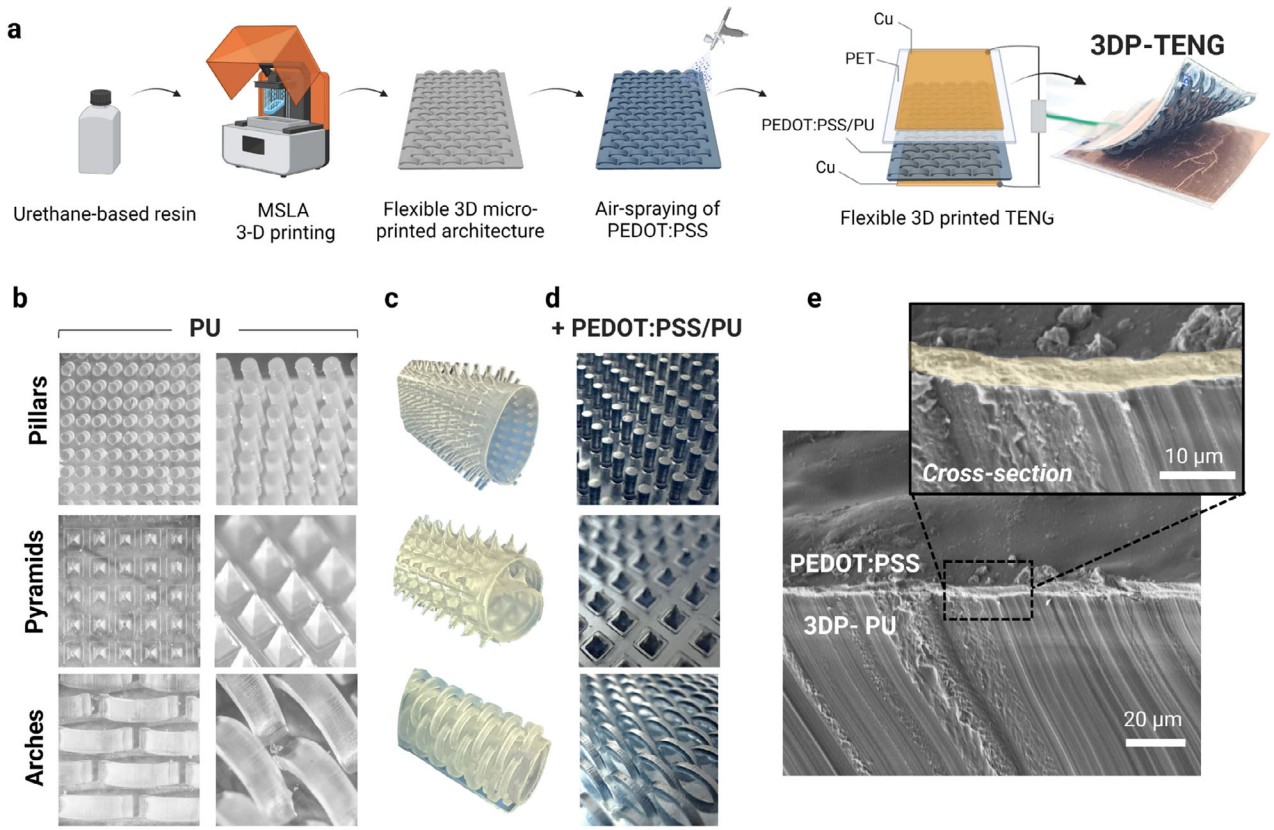

FIGURE 1 | (a) A schematic showing the fabrication process for the 3DP microstructured tribolayers and an illustration of the TENG device architecture. Photograph of a flexible 3DP-TENG based on an arch-structured tribolayer paired with a PET film. Both tribolayers used a Cu-adhesive-based electrode. (created with *Biorender*) (b) Optical microscopy images at various magnifications reveal the pristine 3D microstructures, including pillars, pyramids, and arches. (c) Photographic Images showcasing the flexibility and foldability of the pristine 3DP layers. (d) Photographic images of the P:P spray-coated 3DP structures. (e) SEM image showing a cross-section of the P:P layer on top of the pristine 3DP structures.

patterns using CAD software, samples measuring 50 × 50 mm^2 are 3D-printed, incorporating various shaped microstructures on a thin and flexible support base of ~100 µm. The base layer facilitated sufficient structural integrity and ensured integration into a TENG device format. Subsequently, following plasma UV treatment, the structures are spray-coated with a P:P film between 4 and 5 µm thick and then annealed to enhance film stability and electrical conductivity. The resulting 3DP tribolayer is then integrated into different TENG device configurations, including two-electrode and "zero gap" (ZG)architectures. Figure 1b shows the uncoated 3DP microstructures prepared here, including pillars, pyramids, and arches. Optical microscopy inspection reveals continuous and precisely patterned motifs with dimensionally consistent features over the printed area. The intrinsic flexibility of the photocurable resin, combined with the tailored 3DP design, enabled the fabrication of foldable and mechanically robust microstructured layers, as shown in Figure 1c. As shown in Figure S1, the structures demonstrate mechanical flexibility and rollability, allowing conformal adaptation to non-planar surfaces and repeated rolling about their axis without visible degradation or breakage.

Building on previous studies where P:P is being employed as an electrode or as a charge-transport layer in energy-harvesting devices [46], we herein apply a P:P coating onto the 3DP microstructures to investigate its role in enhancing triboelectric performance (Figure 1d). Air-brush spraying has been chosen for its ability to achieve conformal coating over complex surface geometries without compromising the micromorphology of the 3DP features. By atomizing the P:P solution into fine droplets, the sprayer facilitates complete coverage, allowing penetration into recessed regions and consistent deposition even on high-aspect-ratio architectures. This leads to the formation of continuous, µm-thick P:P films. Unlike other conventional deposition methods, such as spin coating or dip coating, which are well-suited for flat substrates but often lead to non-uniform coverage, poor adhesion, or incomplete film formation on textured surfaces, spraying offers superior adaptability to complex 3D topographies. Particularly in the case of high-aspect-ratio structures, such as those used in our work. Upon optimization, we observe that above 12 sequential spraying passes, a continuous P:P layer is formed over the structures. In such a case, the thickness is estimated to be in the range of 4–5 µm, (see Figure 1e), confirming the formation of a complete P:P layer onto 3DP microstructures.

2.2 | Mechanical Analysis of the Microstructures

The micro-geometry is critical in optimizing the mechanical response and triboelectric performance of 3DP-TENGs. Table 1

TABLE 1 | Design parameters used for the development of the various 3DP geometries.

Design	ID	CAD design	Cell geometry	Dimensions			#Structures
				D (mm)	H (mm)	S (mm)	
Pillars	C	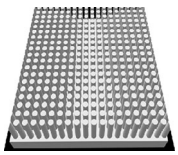	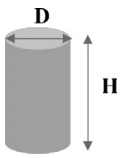	0.5	5	—	400
Pyramids	P	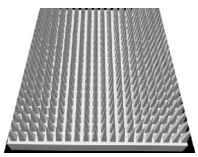	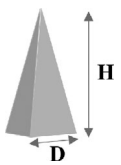	1	5	—	400
Arches	A1	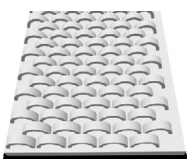	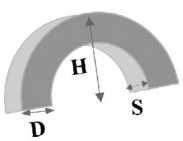	1	4	1.5	95
	A2			0.5	4	1.5	95

summarizes the geometrical parameters of the various 3D printed microstructures, showcasing the different designs and their corresponding unit cell characteristics. Pillar- and pyramid-based tribolayers have been previously studied and are considered promising due to their ability to enhance contact with the surface and maximize the active surface area for effective triboelectrification [24, 47, 48]. On the other hand, the arch design offers a new approach to enhance mechanical response and stability. To macroscopically inspect the effects of localized compression, the 3DP microstructures are subjected to manual compression using a simple hand-press action, as shown in the photographs of Figure 2a. This initiates how the tribolayers respond to vertical pressure, simulating the types of compression stresses expected in wearable or surface-mounted applications. Pillar and pyramid microstructures, while providing relatively high surface area, exhibit limited ability to maintain consistent surface-to-surface interactions. Their response depends strongly on their capacity to deform or bend under pressure, which can influence effective contact with opposing layers. Repeated press–release cycles (via automated mechanical actuator) are found to further compromise their structural integrity, leading to fatigue, most notably in the pillars, where collapse or detachment from the substrate can be observed (see Figure 2b). In contrast, the arches appear to be fatigue-resistant, which can be attributed to their curved geometry that induces a spring-like behavior. This geometry distributes mechanical stresses more evenly and exhibits superior elasticity and recovery compared with other microstructures. As a result, the arches provide a cushioning effect that enhances durability under repeated loading while maintaining consistent surface contact.

The results of monotonic compression tests on the four microstructural types are shown in Figure 2c. The load–displacement curves reveal a clear dependence on geometry. As expected, the pillars exhibit the highest stiffness, owing to their larger cross-sectional area, which resists compressive loads, and their response is nearly linear across the loading range. Pyramid structures exhibit lower stiffness due to their tapering cross-section. In contrast, the arch structures display a more gradual deformation profile. This distinct behavior arises because, under transverse compression, the arches deform mainly through bending rather than buckling. Among the two arch designs investigated, A2 exhibits a lower load–displacement response than A1, which is likely attributable to its smaller cross-sectional area (*D)(*see Table 1).

Cyclic compression has also been performed to test the structural resilience of the 3DP tribolayers up to four cycles (see Figure 2d–g). The arch structures are found to recover more efficiently between cycles, maintaining their ability to resist subsequent loading. In contrast, pillars and pyramids exhibit pronounced hysteresis, particularly the pillars, which carry progressively less load after the first cycle and do not fully recover. This finding highlights the advantages of arch geometries, which combine a large contact area with improved elasticity and recovery, thereby enabling more effective charge generation through the triboelectrification effect.

2.3 | TENG Performance Characteristics

To identify the most effective triboelectric pairing, P:P-coated 3DP tribolayers are tested against various counter materials, including paper, polydimethylsiloxane (PDMS), polyimide (PI), and polyethylene terephthalate (PET) (Figure S2). Among these, PET exhibited the highest performance, generating significantly higher voltage out than PI, the next best-performing material. Figure 3a illustrates the operating principle of the two-electrode TENG device, which employs P:P-coated 3DP arches and PET as the tribolayers operating in a contact–separation mode. Specifically, in the initial state, when the two layers are apart, no charge is present; however, upon contact, triboelectric charges are

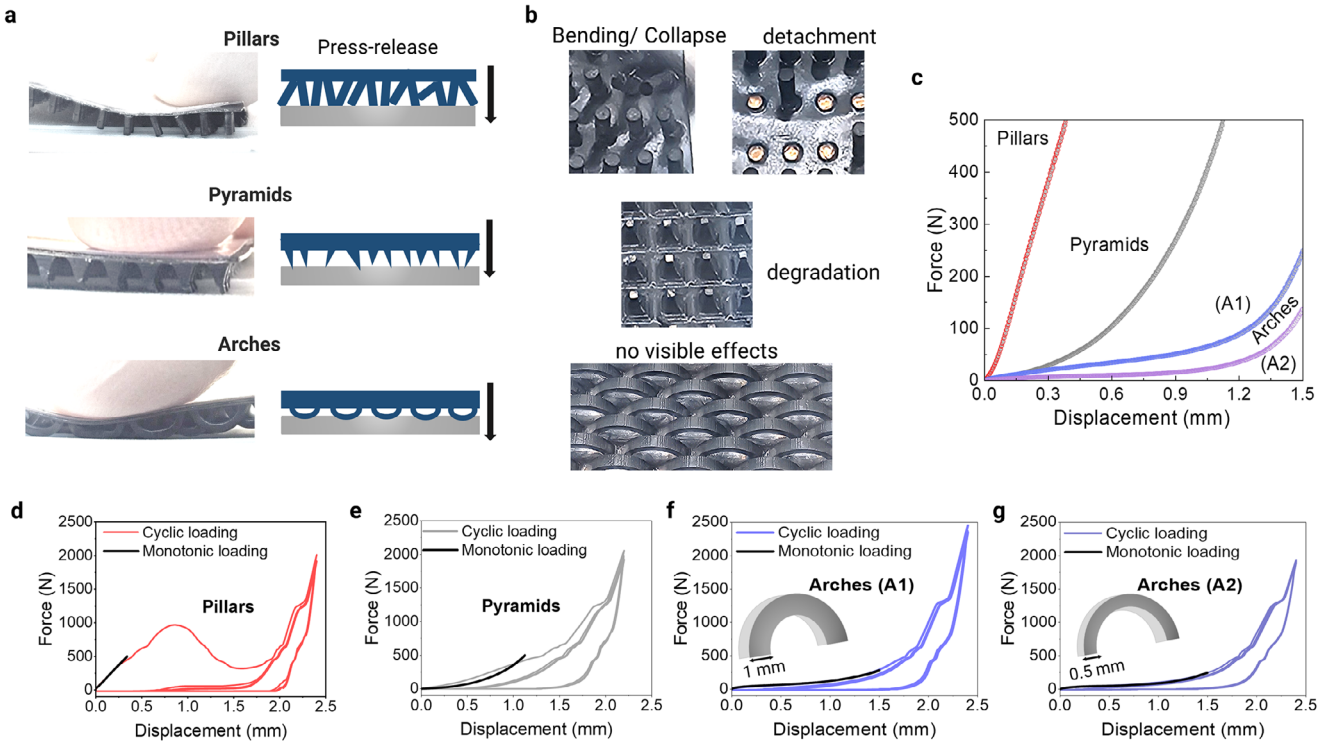

FIGURE 2 | (a) Photographs showing the response of the 3DP microstructures upon vertical compression using finger-pressing action. Illustrations describing the observed feedback effect upon pressure. (b) The corresponding photographs show the degradation effects on the various structures resulting from continuous (> 5000 cycles) press-release cycles. (c) Monotonic compression measurements for the corresponding samples (the test was stopped at 500 N or 1.5 mm displacement to avoid excessive compression of the microstructures). (d–g) Cyclic compression tests of four cycles for the pillars, pyramids, and the two arch types.

generated at the interface between the two surfaces. As the layers separate, a potential difference is established, causing electrons to flow between the two electrodes until equilibrium is reached. When re-contacting the two tribolayers, the induced charges flow back through the external load to balance the potential difference. Therefore, continuous contact and separation cycles cause an AC-like signal output.

To assess the effect of P:P, we first examine the performance of uncoated 3DP tribolayers (see Figure 3b–e). These TENGs, when PET is used as a counter tribolayer, exhibit an overall low voltage output, with a maximum peak of approximately 5.3 V (at 8 Hz) and only minor differences across the tested structures. In contrast, the introduction of a P:P coating significantly enhances TENG performance, as shown in Figure 3f–i. We hypothesize that the P:P coating may alter the roughness surface, creating more active sites for triboelectric interactions and thereby enhancing charge generation efficiency. At the same time, it can store and transfer the generated charges more efficiently, reducing energy losses and amplifying the triboelectrification effect. Clear differences can be observed among the various structural geometries. Specifically, the pillar and pyramid designs are found to reach peak voltages of 15.6 and 11.9 V, respectively. Notably, arch-based TENGs demonstrate superior performance, with types A1 and A2 generating peak voltage outputs of ~66.6 and 101.3 V, respectively. The significant difference in the voltage output can be attributed to their geometry, which enables more effective surface contact during compression and separation.

The influence of surface-to-surface interaction is further evident when comparing A1 and A2. During compression, the arch flattens, increasing the effective contact area, while upon release, it returns to its curved state, retaining triboelectric charges until the next cycle. The thinner cross-section of the A2 arches (denoted as *D* in Table 1) provides better flexibility, which in turn enhances the charge generation and transfer efficiency compared to the thicker A1 arch profile. For comparison, a flat (unstructured) P:P-coated PU tribolayer has also been tested in a TENG configuration. As shown in Figure S3, the device yielded a peak voltage of 44.0 V, significantly lower than the outputs of the arch-based designs, confirming the critical role of surface structuring in triboelectric performance.

As the arch-based TENGs exhibit the most favorable performance among the investigated geometries, further electrical characterization is conducted. Figure 4a,b shows the frequency-dependent voltage outputs for the A1 and A2 TENG configurations, respectively. As the operating frequency increases (from 6 to 10 Hz), both A1 and A2 exhibit a rise in output voltage reflecting the frequency-responsive behavior, typical in TENGs during dynamic mechanical excitation. This enhancement can be attributed to the greater charge accumulation occurring within each cycle at higher frequencies, as well as the increased number of contact–separation events per unit time, which together amplify the total output. In addition, long-term stability is then evaluated through durability tests on both A1 and A2 devices under repeated contact–separation cycles. Specifically, voltage output is monitored by recording 20 s samples every five minutes over a

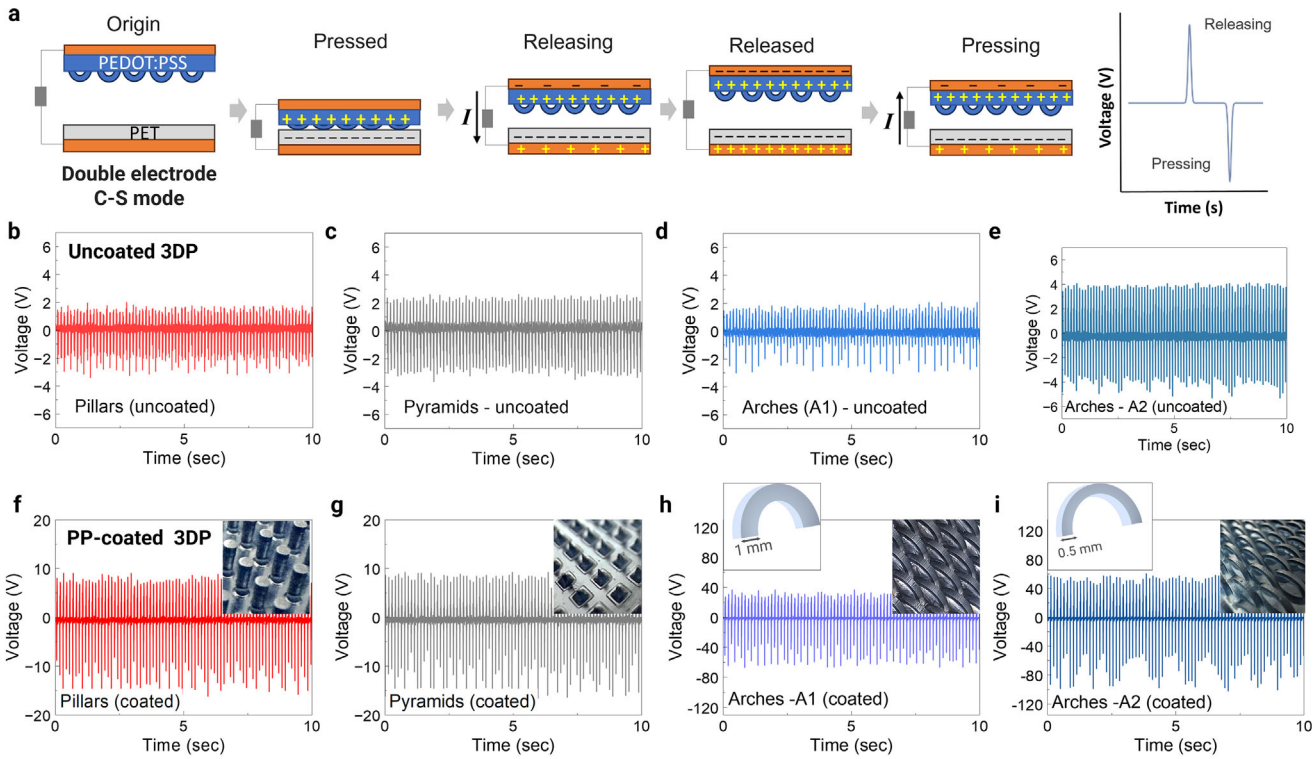

FIGURE 3 | (a) Schematic of the TENG device and its operation, with plots illustrating the TENG voltage output generated for the various 3DP tribolayers (at 8 Hz). A displaying peak generation during press-release actions. (b–e) Voltage output measurements for the uncoated and (f–i) P:P-coated 3DP pillars, pyramids, and arches. Insets display photographic images of the 3DP structures. In the case of 3DP arches, two different dimension conditions (A1 and A2) are tested as indicated in the corresponding insets.

total of 60 min (~28.800 cycles) (see Figure 4c,d). The A1 TENG is found to maintain a stable output, with average peak voltages changing only slightly from −43.2 ± 14.3 V (V_{max} = −63.0 V) to −45.4 ± 14.6 V (V_{max} = −66.8 V) after one hour. In contrast, the A2 devices showed a steady increase in performance, rising from −41.2 ± 11.4 V (V_{max} = −62.0 V) to −67.0 ± 17.9 V (V_{max} = −101.0 V). This behavior is most likely attributed to the enhanced mechanical compliance of A2, which enables adaptation and conditioning to actuation, thereby promoting efficient charge dissipation and voltage generation. To further assess device performance, the transferred charge (Q) is measured for both A1 and A2-based TENGs, as shown in Figure 4e,f. Measurements are carried out at ~6 Hz to ensure stable charge transfer per cycle. Consistent with the voltage measurements, the charge output of the A2 TENG is approximately 33% higher than that of A1, reaching a value of about 46 nC.

The corresponding variations in output power and voltage with different load resistances are shown in Figure 4g,h. In addition, the maximum power output generated is found to be 54.1 mW/m^2 for the A1 and 193.6 mW/m^2 for the A2 TENG, each achieved at its optimal load resistance, indicating the most efficient conditions for power transfer.

To evaluate the effect of compression displacement on the output voltage, the arch-based TENGs (A2) are measured under progressively increasing base height, as shown in Figure S4. As the vertical displacement (D) of the base increases, the separation distance decreases and the overall voltage amplitude is reduced, reaching a plateau beyond a displacement of approximately 4 mm. Under this condition, the arches may not have sufficient time to elastically recover, resulting in a nearly constant effective contact area and thereby limiting further changes in the charge transfer dynamics. The observed plateau indicates that the device has reached its maximum mechanical deformation, beyond which further compression does not result in a significant change in electrical output. It should be noted that the origin position (D = 0 mm) corresponds to the maximum voltage output.

The force-dependent electrical output of the TENG is evaluated by applying two different contact forces, 3 and 8 N, as shown in Figure S5. Under the lower force setting, the device generates a stable but relatively modest voltage output. In contrast, increasing the applied force to 8 N resulted in a significantly enhanced voltage amplitude, to that observed at 3 N. This improvement can be attributed to the increased effective contact area and stronger interfacial interaction between the tribolayers under higher force, which promotes greater triboelectric charge generation.

Furthermore, to assess the durability of the P:P layer under repeated mechanical stress, its electrical and structural stability are examined through sheet resistance measurements and SEM characterization, respectively. As shown in Figure S6a, the average sheet resistance values remain within a comparable range (between 3.4 and 3.9 Ω/sq), and the overall distribution exhibited negligible variation after 10000 cycles, indicating that the electrical conductivity is preserved under repeated mechanical

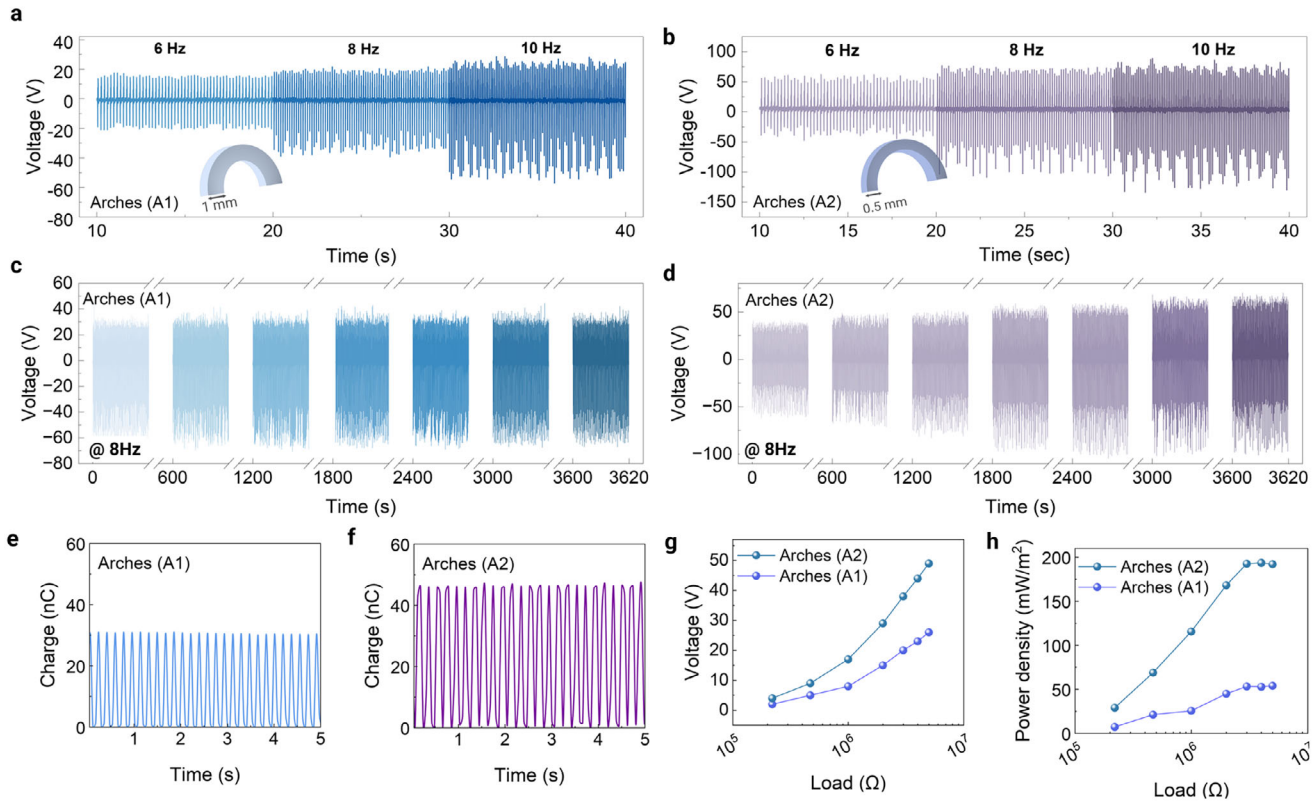

FIGURE 4 | (a) Frequency-dependent TENG output response for the A1 and (b) A2 arch-based TENG. (c) Voltage output response of the 3DP TENG with A1 and (d) A2 arches, showing continuous operation over 60 min. The data were extracted from 20 s recordings every 5 min at 8 Hz. Charge transfer versus time for (e) A1 and (f) A2 based-TENGs. (g) Comparative voltage output and (h) power density output as a function of varying loads for A1 and A2 arch configurations.

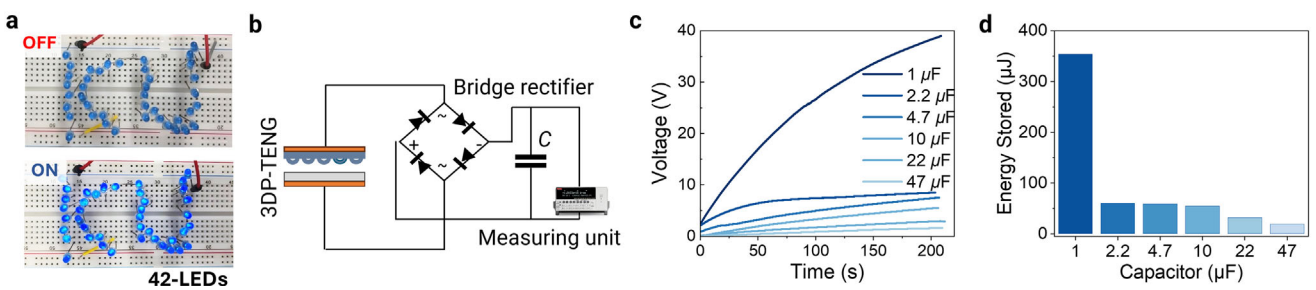

FIGURE 5 | (a) Photograph showing the on/off switching of an array of blue LEDs upon press and release actuation of the 3DP-TENG. (b) The electrical diagram shows the TENG-based capacitor circuit. (c) Capacitor charging curves showing voltage vs. time plots and (d) energy stored using various capacitors, ranging between 1 and 47 μF. The stored energy was estimated over a 100s charge cycle.

activity. In addition, Figure S6b,c presents the SEM images of the P:P-coated microstructures, acquired in top-view configurations, for the freshly coated TENG and after 10000 contact–separation cycles. The post-cycling SEM images reveal no observable cracking, delamination, or surface degradation as compared to the fresh sample, indicating strong interfacial adhesion between the P:P layer and the 3D-printed arches.

Figure 5a demonstrates the energy-harvesting capability of the 3DP-TENG (using the arch design). As shown, the TENG successfully powered an array of 42 blue LEDs (KU logo), which switched *on* and *off* in response to the press–release actuation of the TENG, confirming its ability to convert mechanical energy into electrical output. Figure 5b depicts the schematic of the circuit used to store the generated energy in different capacitors ranging from 1 to 47 μF. The charging characteristics are displayed in Figure 5c, showing the corresponding time-dependent voltage profile. As expected, capacitors with smaller capacitance values appear to charge more rapidly, while those with higher capacitance exhibit a slower voltage rise due to increased storage capacity. Figure 5d shows the calculated energy stored over a 100s charge cycle, revealing that the stored energy decreases with increasing capacitance. Larger capacitors accumulate voltage more slowly, and since the stored energy depends quadratically on voltage, the lower voltage reached within a fixed time results in reduced energy storage.

2.4 | "Zero Gap" Arches TENG

Building on the advantages of the arch geometry, a ZG-TENG is demonstrated in which triboelectrification is driven by the elastic, spring-like motion of the curved structures. This design minimizes the air gap between the triboelectric layers, keeping them in close proximity and simplifying overall device integration and operation. Accordingly, the TENG is designed to maintain a minimal distance between the arch (A2) tribolayer and the PET counter film (Figure 6a). During each press–release cycle, the arch height (h) and contact length (l) dynamically vary, modulating the effective interaction area between the two tribolayers (Figure 6b). With a small residual gap present, the electrical output arises from the same contact electrification and electrostatic induction mechanisms as in conventional contact–separation TENGs. Nevertheless, as shown in Figure 6c, the performance of the ZG-TENGs is significantly lower than that of the typical contact–separation configuration, with the best performing ZG-TENG (A2) exhibiting a voltage of ~14.8 V.

To further clarify the role of separation distance in governing the electrostatic behavior of the ZG-TENG, finite element simulations are performed using COMSOL Multiphysics by varying the gap between the tribolayers from a near-zero separation of 0.5–20 mm. The simulated electric potential distributions are shown in Figure S7. For simplicity, flat-surface geometries are assumed, and microstructural features or surface roughness are neglected to isolate the intrinsic mechanisms of charge transfer and electric-field evolution. Specifically, at near-zero separation, the electric potential is more localized at the contact interface, leading to a weaker potential gradient and limited electrostatic induction due to rapid charge compensation between the opposing triboelectric surfaces. As the separation distance increases, the potential difference between the electrodes becomes more pronounced, accompanied by a spatially extended electric field distribution. Thus, at larger gaps, a strong electric field is established across the device, significantly enhancing electrostatic induction and charge transfer efficiency. These simulation results are consistent with experimental observations and confirm the lower output performance of ZG-TENGs relative to conventional contact–separation TENG configurations. Future work will investigate the dynamic electromechanical response of the arch-based tribolayers using time-dependent coupled simulations. This will capture deformation-driven contact evolution and transient charge redistribution, enabling closer correlation with experimental performance.

2.5 | Wireless Parking Counter Platform

As a proof of concept, the ZG-TENG described in the previous section is used to fabricate a wireless parking sensor capable of transmitting signals to an IoT interface and a counter application. The device operates through a press–release mechanism, generating electrical signals in response to mechanical stimuli such as vertical compression. Figure 6d illustrates the system setup, showing the integration of the TENG sensor, measurement unit, transmitter, and receiver. The sensor unit consists of an arch-based ZG-TENG, a full-wave bridge rectifier, and a voltage divider. Upon mechanical activation, the TENG produces an alternating electrical signal, which is rectified and processed by an Arduino (ESP32) microcontroller, which then wirelessly transmits the data to receiver units via Bluetooth or Wi-Fi. The wireless transmission remains stable across repeated operations, enabling real-time signal detection with rapid response times suitable for event-based pressure sensing. The receiver interprets the incoming signal and triggers a corresponding feedback action on an events counter platform. The system is first evaluated under random mechanical activations (hand tapping) in a laboratory environment, demonstrating high detection accuracy and consistent event recognition (Figure 6e,f). The prototype is further deployed in a designated parking area, where the ZG-TENG is affixed to the road surface (Figure 6g). When a vehicle passes over the device, the generated voltage pulse is reliably detected, activating the LED indicator (Figure 6h; Video S1). The LED switches on when the front tire contacts the sensor and turns off as the rear tire leaves, with each on–off cycle corresponding to a single vehicle passage. This response enables accurate vehicle counting and seamless integration with a monitoring interface accessible via mobile devices or laptops. Overall, the ZG-TENG demonstrates stable, repeatable operation under practical loading conditions, sustaining multiple vehicle passes with high counting reliability. Its robust structural integrity, mechanical flexibility, and wireless compatibility highlight the potential of the 3DP-TENG platform for durable, maintenance-free sensing in smart infrastructure and IoT-based monitoring applications.

3 | Conclusions

This study presents a two-step fabrication strategy for TENGs that combines SLA 3D printing with spray coating of a conductive P:P layer. This approach enables the production of flexible 3DP structured layers with well-defined architectures. Among the tested geometries, the arch design demonstrated the highest performance, offering better mechanical adaptability and contact efficiency, which resulted in higher voltage and power outputs compared to conventional pillar and pyramid structures. The P:P coating further improved device performance by enhancing surface conductivity and charge transfer. The elastic, spring-like response of the arches also enabled the realization of a compact ZG-TENG suitable for compression-based sensing and wearable systems. Device operation was demonstrated using a wireless parking sensor prototype, which maintained stable detection accuracy under repeated mechanical loading. As summarized in Table S1, the proposed device outperforms previously reported TENGs fabricated by filament 3D printing, DIW, and SLA, with our 3DP approach delivering a superior voltage output. From an application standpoint, the device can be readily integrated into high-load and highly sensitive environments, enabling real-time energy harvesting and sensing for smart infrastructure, transportation, and health monitoring systems.

4 | Experimental Section/Methods

4.1 | Materials

For the fabrication of the 3DP structures, a commercial polyurethane-based resin (57.7% urethane acrylate, 38%

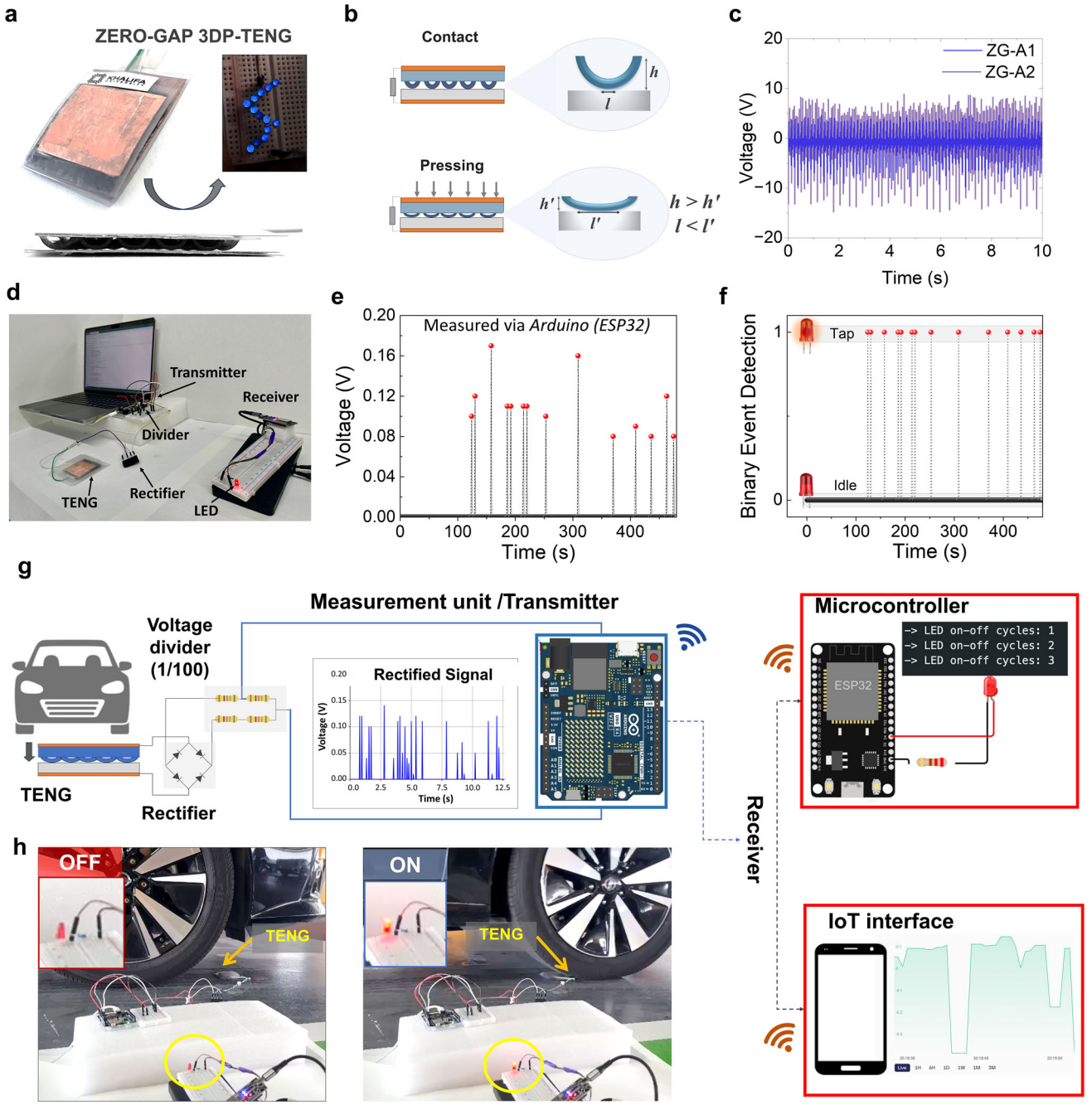

FIGURE 6 | (a) Photograph of a ZG-TENG device composed of a P:P-coated 3DP (A2) and a counter PET tribolayer. (b)The schematic illustrates the ZG operation, which involves uncompressed and compressed states. Zoomed drawings highlight the dimensional changes of the arches upon compression. (c) Plots showing the voltage output upon press-release action of ZG-A1 and ZG-A2 devices. (d) Photograph showing the laboratory setup and the components used for wireless transmission of pressure-sensing signals generated by hand tapping. (e) Graph showing the voltage signal recorded by an Arduino (ESP32 microcontroller). The signal is divided by a factor of 100 using a voltage divider circuit. (f) Binary event detection timeline of the wireless ZG-TENG system showing individual activation events. The device maintained 100% detection accuracy across repeated cycles, indicating idle states (LED off) and active states (LED on) upon actuation (tapping). (g) Schematic of the ZG-based TENG pressure sensor integrated with an interconnected counter system, comprising a rectifier, voltage divider, wireless Arduino-based signal transmitter, receiver modules, a microcontroller for LED switching, and a mobile interface for data recording. (h) Photographs of the TENG sensor embedded in a roadbed, showing the OFF state (no car detected) and the ON state (car passes). Upon vehicle passage, the TENG generates a signal that is wirelessly transmitted to the microcontroller, which in turn triggers the LED indicator as shown in the inset.

acrylate monomer, 4% photoinitiator) (Siraya Tech Tenacious) was purchased and used as is. The P:P solution is composed of poly(3,4-ethylenedioxythiophene):poly(styrene sulfonate) (Heraeus, Clevios PH1000), Ethylene Glycol (Sigma–Aldrich), 4-dodecylbenzenesulfonic acid (DBSA) (Sigma–Aldrich), and 3-glycidoxypropyltrimethoxysilane (GOPS) (Sigma–Aldrich).

4.2 | TENG Layers Design and Characterization

The main layer of the TENG was designed and printed with three different surface microstructures, all with a base layer thickness of ∼100 μm and base dimensions of 50 mm by 50 mm, using AutoCAD software. Pillars and pyramids were designed with aligned geometries, while the novel arches were designed with alternating geometries and varying dimensions. The layers were then sliced using Chitobox software for 3D printing. The layers were 3D printed using photopolymer polyurethane resin, known for its flexibility and high impact resistance, on an ELEGOO Mars 3 Pro Resin stereolithography 3D printer. After printing, the structures were washed and cured with isopropyl alcohol using the ELEGOO Mercury Plus 2-in-1 Washing and Curing Machine. This process ensured the quality and durability of the printed layers, completed the polymerization, and stabilized the dimensions of the printed layers. For the layer optimization, an initial analysis of the PU-printed structures was conducted both optically and mechanically to evaluate their performance. Optical analysis, performed using a Leica M165 FC Optical Microscope, was critical for detecting defects, evaluating the uniformity of the microstructures, and accurately measuring dimensions to verify conformity with design specifications. For the mechanical analysis, a SALT Universal Testing Machine was used under the following test conditions: a displacement limit of 3.5 mm, a constant loading rate of 1 mm/min, and compression to a maximum applied load of 5 kN. The compression test was essential for assessing the microstructure's strength and durability, particularly under repeated deformation cycles. This test provided insights into the material's deformation and failure modes, identifying how it deforms under different loads and determining its failure points.

4.3 | Preparation and Deposition of P:P Solution

4.3.1 | P:P Solution Preparation

The P:P solution was prepared following a previously published process route [49]. Initially, the solution was filtered through a locked-lude syringe equipped with a 0.45 PTFE filter to remove any aggregates and achieve uniformity. 5 wt.% ethylene glycol was added to improve conductivity, followed by ultrasonication at room temperature for 10 min. Next, 0.5 wt.% DBSA was added, and the mixture was ultrasonicated for an additional 10 min to enhance stability. Finally, 1 wt.% GOPS was incorporated and ultrasonicated for another 10 min to cross-link PEDOT:PSS. The final solution underwent a second filtration to ensure the formation of a high-quality conductive layer.

4.3.2 | Surface Treatment

Before the spray coating process, all the 3DP structures underwent plasma treatment to improve surface adhesion, ensuring that the P:P layer adhered uniformly and firmly to the substrate. Pillars, pyramids, and arches were treated for comparative purposes. The treatment was conducted under vacuum with oxygen, maintaining chamber pressure between 1000 and 1100 Pa for 3 min. This critical step modified the surface properties of the 3DP layers by introducing functional groups that enhanced the adhesion of the P:P coating.

4.3.3 | P:P Deposition

The final step entails applying the P:P solution to the treated 3DP structures using a spray coating technique. An airbrush was utilized to apply the solution layer by layer, with a total of 12 layers being sprayed at an angle. Each layer consisted of horizontal and vertical passes, enabling uniform coverage of the entire microstructure, and was allowed to dry completely before the next layer was sprayed, ensuring optimal adhesion. This was accomplished by placing the coated structure on a hot plate set at 60°C for approximately 1 min. This iterative spraying and drying process ensures a uniform conductive layer is formed.

4.4 | Mechanical Characterization

All the samples of TENG containing various microstructure geometries were tested under compression loading conditions. Following a previously published methodology, an Intron UTM Model 5969 with a 5 kN load cell capacity was used for these tests [50]. The tests were conducted in a displacement-controlled mode, where both monotonic and cyclic tests were performed at a displacement rate of 1 mm/min. During the monotonic tests, a maximum compression displacement of 1.5 mm and 500 N was set as the test termination criteria. On the other hand, the microstructure geometries were tested for higher displacement and load values in cyclic loading than the monotonic tests to evaluate the structural integrity and recovery for higher loading conditions. The samples were placed at the center of the lower stationary compression platen, where the microstructures faced the upper loading compression platen. The upper platen was carefully positioned to be in contact with the microstructures of the sample, maintaining a pre-load of ∼10 N, which was balanced before the commencement of each compression test. Moreover, each test was repeated at least three times to record the experimental scatter. A representative load vs. displacement curve for each test is presented.

4.5 | TENG Device Fabrication and Characterization

The 3DP microstructure layers and PET film were placed on top of copper (Cu) tape to construct the triboelectric pair, which served as electrodes. The triboelectric layers were positioned facing each other to create a TENG with an active area of 50 × 50 mm^2.

The TENGs operated in two modes: initially, in contact and separation mode, applying continuous physical motion between the two surfaces with a distinct separation gap (See Figure 1a), and second, in a zero-gap mode, where the devices functioned as a single component with minimal gap, presenting a smaller form factor (See Figure 1b). The voltage output generated by the TENGs was measured by attaching both layers to an automated linear actuator to simulate repetitive mechanical tapping. The voltage output was recorded using a digital oscilloscope (Tektronix TDS 3034C) operating at 300 MHz with a sampling rate of 2.5 GS/s. The transferred charge and the voltage output for various capacitors were measured using a Keithley 6517B electrometer. The instrument operation was controlled through a LabVIEW interface for data acquisition and storage.

4.6 | TENG Simulations

Electrostatic simulations were performed using COMSOL Multiphysics to investigate the effect of separation distance on the electrical behavior of TENG devices. A 2D electrostatics model was employed, consisting of two opposing tribolayers with flat surfaces to simplify the geometry and isolate the fundamental charge transfer mechanisms. The model parameters include the thicknesses of tribolayers, PET (100 μm) and printed layer (500 μm), P:P (5 μm), as well as their corresponding Cu electrode layers (100 μm), with material properties assigned according to literature-reported dielectric constants. The separation distance between the tribolayers was varied from a near-zero gap (0.5 mm) to 20 mm.

4.7 | Wireless Transmission System Using the 3DP-TENG

The wireless system for the 3DP-TENGs comprises transmission and receiver modules that are connected for efficient data handling and stability. The transmission circuit transmits data based on the voltage generated by the TENG, which is enabled via contact or tapping activity. The TENG produces an alternating voltage during operation, which is then rectified into direct voltage for compatibility. A microcontroller with WiFi/Bluetooth capabilities and a voltage divider circuit ensures that the microcontroller operates at safe voltage levels. The transmission circuit utilizes an Arduino R4 Bluetooth/WiFi microcontroller, capable of transmitting data via WiFi or Bluetooth signals. The microcontroller operates at a maximum voltage of 5 V. A voltage divider circuit comprising of four resistors was used to effectively reduce the TENG-generated voltage by a factor of 100, ensuring compatibility with the microcontroller. The rectifier was used to generate a unipolar output voltage, ensuring that only positive signals were introduced to the system, thereby ensuring more reliable operation. The voltage generated by the TENG is converted into an electronic signal and transmitted to a receiver circuit for processing. The receiver circuit incorporates an ESP32 microcontroller, which facilitates data communication through WiFi or Bluetooth. A custom program was written to ensure connectivity between the transmitting and receiving microcontroller units (through WiFi), allowing the voltage signal to be utilized for the tested applications. The received signal was used for the counter system to control an LED, enabling it to turn on and off in response to the feedback received, effectively functioning as a parking sensor.

Author Contributions

M. E. Alhosani: conceptualization (equal), validation (equal), investigation (equal), data curation (equal), formal analysis (equal), writing – original draft (equal), writing – review and editing (supporting). **B. Fatma**: conceptualization (equal), data curation (equal), formal analysis (equal), investigation (equal), writing – original draft (equal), writing – review and editing (equal). **R. B. Irshaid**: investigation (supporting), formal analysis (supporting). **K. Katsikari**: investigation (supporting), formal analysis (supporting). **S. Kang**: investigation (supporting), **Y. P. Jeon**: investigation (supporting). **M. Aljaberi**: conceptualization (supporting), validation (supporting). **I. U. Din**: investigation (supporting), formal analysis (supporting). **K. A. Khan**: formal analysis (supporting), funding acquisition (supporting), investigation (supporting). **C. Pitsalidis**: conceptualization (supporting); formal analysis (supporting); funding acquisition (lead), investigation (equal); project administration (lead), visualization (equal), resources (lead), writing – original draft (equal); writing – review and editing (equal).

Acknowledgements

This project is supported by Multiple Sclerosis Society UAE (NMSS, Project: Sense-MS 8434000661). This work is funded by the Advanced Research and Innovation Center (ARIC), which is jointly funded by Aerospace Holding Company LLC, a wholly owned subsidiary of Mubadala Investment Company PJSC, and Khalifa University of Science and Technology. This work is also supported by the Advanced Institute of Convergence Technology and the Next Generation Intelligence Semiconductor Foundation grant funded by the Korea government (MOTIE, 20023508) and the National Research Foundation grant funded by the Korea government (MSIT, RS-2024-00411892).

Conflicts of Interest

The current development has been submitted for a patent application.

Data Availability Statement

The data that support the findings of this study are available from the corresponding author upon reasonable request.

References

1. H. Kim, K. R. Pyun, M. Lee, H. B. Lee, and S. H. Ko, "Recent Advances in Sustainable Wearable Energy Devices with Nanoscale Materials and Macroscale Structures," *Advanced Functional Materials* 32 (2022): 2110535, https://doi.org/10.1002/adfm.202110535.

2. H. Ryu, H. Yoon, and S. Kim, "Hybrid Energy Harvesters: Toward Sustainable Energy Harvesting," *Advanced Materials* 31 (2019): 1802898, https://doi.org/10.1002/adma.201802898.

3. D. Tao, P. Su, A. Chen, D. Gu, M. Eginligil, and W. Huang, "Electro-Spun Nanofibers-Based Triboelectric Nanogenerators in Wearable Electronics: Status and Perspectives," *npj Flexible Electronics* 9 (2025): 4, https://doi.org/10.1038/s41528-024-00357-5.

4. P. Pandey, P. Maharjan, M.-K. Seo, K. Thapa, and J. I. Sohn, "Recent Progress in Wearable Triboelectric Nanogenerator for Advanced Health Monitoring and Rehabilitation," *International Journal of Energy Research* 2024 (2024): 5572736, https://doi.org/10.1155/2024/5572736.

5. M. Xu, Y. Mao, and W. Hu, "All-Hydrogel Yarn-Based Supercapacitor Wrapped with Multifunctional Cotton Fiber for Energy Storage and Sensing," *Nano Energy* 130 (2024): 110142, https://doi.org/10.1016/j.nanoen.2024.110142.

6. Y. Mao, Y. Li, J. Xie, H. Liu, C. Guo, and W. Hu, "Triboelectric Nanogenerator/Supercapacitor In-One Self-Powered Textile Based on PTFE Yarn Wrapped PDMS/MnO_2NW Hybrid Elastomer," *Nano Energy* 84 (2021): 105918, https://doi.org/10.1016/j.nanoen.2021.105918.

7. T. Cheng, J. Shao, and Z. L. Wang, "Triboelectric Nanogenerators," *Nature Reviews Methods Primers* 3 (2023): 39, https://doi.org/10.1038/s43586-023-00220-3.

8. H. Wang, J. Cheng, Z. Wang, L. Ji, and Z. L. Wang, "Triboelectric Nanogenerators for Human-Health Care," *Science Bulletin* 66 (2021): 490–511, https://doi.org/10.1016/j.scib.2020.10.002.

9. B. Fatma, I. Ziogas, R. Kumar, et al., "Bioderived and All-Solution-Processed Tribolayer Component Enables Adaptive Design of Flexible Nanocellulosic Triboelectric Nanogenerators," *Journal of Materials Chemistry A* 14 (2025): 4162–4176, https://doi.org/10.1039/d5ta05646b.

10. J. An, Z. M. Wang, T. Jiang, X. Liang, and Z. L. Wang, "Whirling-Folded Triboelectric Nanogenerator with High Average Power for Water Wave Energy Harvesting," *Advanced Functional Materials* 29 (2019): 1904867, https://doi.org/10.1002/adfm.201904867.

11. Y. Li, H. Deng, H. Wu, et al., "Rotary Wind-Driven Triboelectric Nanogenerator for Self-Powered Airflow Temperature Monitoring of Industrial Equipment," *Advanced Science* 11 (2024): 2307382, https://doi.org/10.1002/advs.202307382.

12. X. Pu, M. Liu, X. Chen, et al., "Ultrastretchable, Transparent Triboelectric Nanogenerator as Electronic Skin for Biomechanical Energy Harvesting and Tactile Sensing," *Science Advances* 3 (2017): 1700015, https://doi.org/10.1126/sciadv.1700015.

13. J. Shao, M. Willatzen, and Z. L. Wang, "Theoretical Modeling of Triboelectric Nanogenerators (TENGs)," *Journal of Applied Physics* 128 (2020): 111101, https://doi.org/10.1063/5.0020961.

14. Z. L. Wang, "On the Expanded Maxwell's Equations for Moving Charged Media System—General Theory, Mathematical Solutions and Applications in TENG," *Materials Today* 52 (2022): 348–363, https://doi.org/10.1016/j.mattod.2021.10.027.

15. W.-G. Kim, D.-W. Kim, I.-W. Tcho, J.-K. Kim, M.-S. Kim, and Y.-K. Choi, "Triboelectric Nanogenerator: Structure, Mechanism, and Applications," *ACS Nano* 15 (2021): 258–287, https://doi.org/10.1021/acsnano.0c09803.

16. Y. Luo, Y. Li, X. Feng, et al., "Triboelectric Nanogenerators with Porous and Hierarchically Structured Silk Fibroin Films via Water Electrospray-Etching Technology," *Nano Energy* 75 (2020): 104974, https://doi.org/10.1016/j.nanoen.2020.104974.

17. K. Ghosh, C. Iffelsberger, M. Konečný, J. Vyskočil, J. Michalička, and M. Pumera, "Nanoarchitectonics of Triboelectric Nanogenerator for Conversion of Abundant Mechanical Energy to Green Hydrogen," *Advanced Energy Materials* 13 (2023): 2203476, https://doi.org/10.1002/aenm.202203476.

18. B. Fatma, S. M. Andrabi, S. Gupta, et al., "Biocompatible, Breathable and Degradable Microbial Cellulose Based Triboelectric Nanogenerator for Wearable Transient Electronics," *Nano Energy* 114 (2023): 108628, https://doi.org/10.1016/j.nanoen.2023.108628.

19. K. K. Jena, B. Fatma, S. S. Arya, et al., "High Performance Flexible Triboelectric Nanogenerators Using Bio-Derived Films Made of Siloxane-Modified Castor Oil," *Journal of Materials Chemistry A* 12 (2024): 8340–8349, https://doi.org/10.1039/d3ta05429b.

20. Y. Wang, A. T. T. Pham, X. Han, D. Du, and Y. Tang, "Design and Evaluate the Wave Driven-Triboelectric Nanogenerator Under External Wave Parameters: Experiment and Simulation," *Nano Energy* 93 (2022): 106844, https://doi.org/10.1016/j.nanoen.2021.106844.

21. Y. Wu, Y. Li, Y. Zou, et al., "A Multi-Mode Triboelectric Nanogenerator for Energy Harvesting and Biomedical Monitoring," *Nano Energy* 92 (2022): 106715, https://doi.org/10.1016/j.nanoen.2021.106715.

22. M.-L. Seol, J.-W. Han, D.-I. Moon, K. J. Yoon, C. S. Hwang, and M. Meyyappan, "All-Printed Triboelectric Nanogenerator," *Nano Energy* 44 (2018): 82–88, https://doi.org/10.1016/j.nanoen.2017.11.067.

23. S. Lee and J.-W. Park, "Fingerprint-Inspired Triboelectric Nanogenerator with a Geometrically Asymmetric Electrode Design for a Self-Powered Dynamic Pressure Sensor," *Nano Energy* 101 (2022): 107546, https://doi.org/10.1016/j.nanoen.2022.107546.

24. W. Yang, X. Wang, H. Li, J. Wu, and Y. Hu, "Comprehensive Contact Analysis for Vertical-Contact-Mode Triboelectric Nanogenerators with Micro-/Nano-Textured Surfaces," *Nano Energy* 51 (2018): 241–249, https://doi.org/10.1016/j.nanoen.2018.06.066.

25. J. Son, H. Kim, Y. Choi, and H. Lee, "3D Printed Energy Devices: Generation, Conversion, and Storage," *Microsystems & Nanoengineering* 10 (2024): 93, https://doi.org/10.1038/s41378-024-00708-2.

26. A. Chiappone, I. Roppolo, E. Scavino, G. Mogli, C. F. Pirri, and S. Stassi, "Three-Dimensional Printing of Triboelectric Nanogenerators by Digital Light Processing Technique for Mechanical Energy Harvesting," *ACS Applied Materials & Interfaces* 15 (2023): 53974–53983, https://doi.org/10.1021/acsami.3c13323.

27. B. Chen, W. Tang, T. Jiang, et al., "Three-Dimensional Ultraflexible Triboelectric Nanogenerator Made by 3D Printing," *Nano Energy* 45 (2018): 380–389, https://doi.org/10.1016/j.nanoen.2017.12.049.

28. S. Akin, T. Chang, S. S. H. Abir, et al., "One-Step Fabrication of Functionalized Electrodes on 3D-Printed Polymers for Triboelectric Nanogenerators," *Nano Energy* 129 (2024): 110082, https://doi.org/10.1016/j.nanoen.2024.110082.

29. H. C. Cho, M. Latif, Y. Jiang, and J. Kim, "Environment-Friendly Triboelectric Nanogenerator Based on 3D-Printed Nanocellulose Films for Human Motion Monitoring," *ACS Applied Energy Materials* 8 (2025): 267–275, https://doi.org/10.1021/acsaem.4c02319.

30. M. Wajahat, A. Z. Kouzani, S. Y. Khoo, and M. A. P. Mahmud, "Development of Triboelectric Nanogenerators Using Novel 3D Printed Polymer Materials," *Advanced Engineering Materials* 26 (2023): 2301897, https://doi.org/10.1002/adem.202301897.

31. A. Mohapatra, N. Divakaran, Y. Alex, A. P. V. Kumar, and S. Mohanty, "The Significant Role of CNT-ZnO Core-Shell Nanostructures in the Development of FDM-Based 3D-Printed Triboelectric Nanogenerators," *Materials Today Nano* 22 (2023): 100313, https://doi.org/10.1016/j.mtnano.2023.100313.

32. C. Qian, L. Li, M. Gao, et al., "All-Printed 3D Hierarchically Structured Cellulose Aerogel Based Triboelectric Nanogenerator for Multi-Functional Sensors," *Nano Energy* 63 (2019): 103885, https://doi.org/10.1016/j.nanoen.2019.103885.

33. H. Dong, S. Jiang, H. Wu, et al., "One-Stop Fabrication of Flexible Sensors Based on Aqueous Printable Triboelectric Layer-Electrode Integrated Ink with Enhanced Heat-Resistance," *Advanced Materials Technologies* 8 (2023): 2301022, https://doi.org/10.1002/admt.202301022.

34. H. Li, R. Li, X. Fang, et al., "3D Printed Flexible Triboelectric Nanogenerator with Viscoelastic Inks for Mechanical Energy Harvesting," *Nano Energy* 58 (2019): 447–454, https://doi.org/10.1016/j.nanoen.2019.01.066.

35. B. Nowacki, K. Mistewicz, S. Hajra, and H. J. Kim, "3D Printed Triboelectric Nanogenerator for Underwater Ultrasonic Sensing," *Ultrasonics* 133 (2023): 107045, https://doi.org/10.1016/j.ultras.2023.107045.

36. H.-J. Yoon, D.-H. Kim, W. Seung, et al., "3D-Printed Biomimetic-Villus Structure with Maximized Surface Area for Triboelectric Nanogenerator and Dust Filter," *Nano Energy* 63 (2019): 103857, https://doi.org/10.1016/j.nanoen.2019.103857.

37. Y. Hao, J. Yang, X. Zhu, et al., "PEO/Cysteine Composite Nanofiber-Based Triboelectric Nanogenerators for Harvesting Tiny Mechanical Energy," *Journal of Materials Chemistry A* 13 (2024): 1853–1862, https://doi.org/10.1039/d4ta06845a.

38. W. Cho, S. Kim, H. Lee, et al., "High-Performance Yet Sustainable Triboelectric Nanogenerator Based on Sulfur-Rich Polymer Composite with MXene Segregated Structure," *Advanced Materials* 36 (2024): 2404163, https://doi.org/10.1002/adma.202404163.

39. S. Wu, G. Li, W. Liu, et al., "Fabrication of Polyethyleneimine-Paper Composites with Improved Tribopositivity for Triboelectric Nanogenerators," *Nano Energy* 93 (2022): 106859, https://doi.org/10.1016/j.nanoen.2021.106859.

40. S. Cui, Y. Zheng, J. Liang, and D. Wang, "Conducting Polymer PPy Nanowire-Based Triboelectric Nanogenerator and Its Application for Self-Powered Electrochemical Cathodic Protection," *Chemical Science* 7 (2016): 6477–6483, https://doi.org/10.1039/c6sc02562e.

41. Z. Wen, Y. Yang, N. Sun, et al., "A Wrinkled PEDOT:PSS Film Based Stretchable and Transparent Triboelectric Nanogenerator for Wearable Energy Harvesters and Active Motion Sensors," *Advanced Functional Materials* 28 (2018): 1803684, https://doi.org/10.1002/adfm.201803684.

42. M. H. Chung, H.-J. Kim, S. Yoo, H. Jeong, and K.-H. Yoo, "Enhancement of Triboelectricity Based on Fully Organic Composite Films with a Conducting Polymer," *RSC Advances* 12 (2022): 2820–2829, https://doi.org/10.1039/d1ra07408c.

43. S. Lan, Y. Mao, B. Zhou, and W. Hu, "PEDOT-Molecular Bridging Foam-Hydrogel Based Wearable Triboelectric Nanogenerator for Energy Harvesting and Sensing," *Nano Energy* 134 (2025): 110572, https://doi.org/10.1016/j.nanoen.2024.110572.

44. M. Kim, S. Lee, V. A. Cao, M. C. Kim, and J. Nah, "Performance Enhancement of Triboelectric Nanogenerators via Photo-Generated Carriers Using a Polymer-Perovskite Composite," *Nano Energy* 112 (2023): 108474, https://doi.org/10.1016/j.nanoen.2023.108474.

45. B.-Y. Lee, S.-U. Kim, S. Kang, and S.-D. Lee, "Transparent and Flexible High Power Triboelectric Nanogenerator with Metallic Nanowire-Embedded Tribonegative Conducting Polymer," *Nano Energy* 53 (2018): 152–159, https://doi.org/10.1016/j.nanoen.2018.08.048.

46. H. Yoon, H. Ha, C. Choi, T. G. Yun, and B. Hwang, "Mini Review on PEDOT:PSS as a Conducting Material in Energy Harvesting and Storage Devices Applications," *Journal of Polymer Materials* 40 (2023): 1–17, https://doi.org/10.32381/jpm.2023.40.1-2.1.

47. J. Wang, S. Qian, J. Yu, et al., "Flexible and Wearable PDMS-Based Triboelectric Nanogenerator for Self-Powered Tactile Sensing," *Nanomaterials* 9 (2019): 1304, https://doi.org/10.3390/nano9091304.

48. H. Feng, H. Li, J. Xu, et al., "Triboelectric Nanogenerator Based on Direct Image Lithography and Surface Fluorination for Biomechanical Energy Harvesting and Self-Powered Sterilization," *Nano Energy* 98 (2022): 107279, https://doi.org/10.1016/j.nanoen.2022.107279.

49. J. Pas, C. Pitsalidis, D. A. Koutsouras, et al., "Neurospheres on Patterned PEDOT:PSS Microelectrode Arrays Enhance Electrophysiology Recordings," *Advanced Biosystems* 2 (2018): 1700164, https://doi.org/10.1002/adbi.201700164.

50. I. U. Din, S. S. Kulkarni, and K. A. Khan, "Thermo-Mechanical Viscoelastic Characterization and Modeling of 4D Printed Shape Memory Polymers," *Polymer Testing* 143 (2025): 108708, https://doi.org/10.1016/j.polymertesting.2025.108708.

Supporting Information

Additional supporting information can be found online in the Supporting Information section.

Supporting File 1: admi70451-sup-0001-SuppMat.docx.

Supporting File 2: admi70451-sup-0002-VideoS1.mp4.